PAPER

Check for updates

Anisotropic mechanical properties of α-MoO₃ nanosheets†

Congying Wang,[a,b] Xuwei Cui,[a,c] Shijun Wang,[a] Wenlong Dong,[a,b] Hai Hu,[d]
Xiaoyong Cai,[d] Chao Jiang,[d] Zhong Zhang*[c] and Luqi Liu ⓘ *[a,b]

The mechanical behaviors of 2D materials are fundamentally important for their potential applications in various fields. α-Molybdenum trioxide (α-MoO₃) crystals with unique electronic, optical, and electrochemical properties, have attracted extensive attention for their use in optoelectronic and energy conversion devices. From a mechanical viewpoint, however, there is limited information available on the mechanical properties of α-MoO₃. Here, we developed a capillary force-assisted peeling method to directly transfer α-MoO₃ nanosheets onto arbitrary substrates. Comparatively, we could effectively avoid surface contamination arising from the polymer-assisted transfer method. Furthermore, with the help of an *in situ* push-to-pull (PTP) device during SEM, we systematically investigated the tensile properties of α-MoO₃. The measured Young's modulus and fracture strengths along the *c*-axis (91.7 ± 13.7 GPa and 2.1 ± 0.9 GPa, respectively) are much higher than those along the *a*-axis (55.9 ± 8.6 GPa and 0.8 ± 0.3 GPa, respectively). The in-plane mechanical anisotropy ratio can reach ~1.64. Both Young's modulus and the fracture strength of MoO₃ show apparent size dependence. Additionally, the multilayer α-MoO₃ nanosheets exhibited brittle fracture with interplanar sliding due to poor van der Waals interaction. Our study provides some key points regarding the mechanical properties and fracture behavior of layered α-MoO₃ nanosheets.

Introduction

Thermodynamically stable molybdenum trioxide (α-MoO₃) consists of bilayer planar crystals of distorted MoO₆ octahedra, in which the internal linkages are formed by covalent bonds and adjacent layers are held by weak van der Waals forces.[1,2] As a promising anisotropic layered crystal phase, α-MoO₃ with wide tunable bandgap, high electron mobility, and excellent photoelectric properties, has attracted immense attention in the fields of optoelectronics, flexible electronic devices and energy conversion devices.[3–5] A comprehensive understanding of the mechanical properties of α-MoO₃ is essential to fulfilling its potential applications. Given that the properties of elas-

ticity, bending ability, fracture strength, and stretchability of α-MoO₃ are heavily orientation-dependent,[6,7] the reliability of devices based on α-MoO₃ nanosheets would be greatly affected by their mechanical responses. However, there has been limited information available on the mechanical properties and failure mechanism of α-MoO₃.

Over the past decade, several testing methods have been developed to explore the mechanical properties of 2D materials, such as atomic force microscopy (AFM) nanoindentation methods,[8–11] micro-electro-mechanical systems (MEMS)-based *in situ* tensile testing,[12–14] blister testing,[15–18] and so on.[19,20] For example, AFM-based nanoindentation is a technique that was first used to determine the modulus and breaking strength of freestanding monolayer graphene.[8] The blister test is employed to study Young's modulus and bending stiffness of various 2D crystals involving graphene, MoS₂, and so on.[15,17,21,22] The *in situ* tensile test, as a direct testing method, allows precise measurement of crystal orientation-dependent mechanical parameters of 2D materials.[7,14,23] Additionally, it facilitates the observation of deformation behaviors in response to applied strain.[13,14,24] One of the major challenges of *in situ* nanomechanical tensile tests lies in precise manipulation and then successful transfer of the ultra-thin 2D membrane onto the target device (*e.g.*, push-to-pull (PTP)). To date, the most frequently employed strategy is the

[a]CAS Key Laboratory of Nanosystem and Hierarchical Fabrication and CAS Center for Excellence in Nanoscience, National Center for Nanoscience and Technology, Beijing, 100190, China. E-mail: liulq@nanoctr.cn
[b]University of Chinese Academy of Sciences, Beijing, 100049, China
[c]CAS Key Laboratory Mechanical Behavior and Design of Materials, Department of Modern Mechanics, University of Science and Technology of China, Hefei, 230027, China. E-mail: zhangzhong@ustc.edu.cn
[d]CAS Key Laboratory of Standardization and Measurement for Nanotechnology and CAS Center for Excellence in Nanoscience, National Center for Nanoscience and Technology, 100190 Beijing, China
†Electronic supplementary information (ESI) available. See DOI: https://doi.org/10.1039/d3nr06427a

polymer-assisted transfer approach,[24,25] followed by subsequent heating/washing treatments to remove polymeric contamination. However, the presence of polymer residuals is inevitable and affects the mechanical responses of 2D materials.[26] Therefore, it remains challenging to develop a novel transfer method to prepare clean test samples with high efficiency.

In this work, we developed a capillary force-assisted peeling method to directly transfer individual α-MoO$_3$ nanosheets onto the target device in liquid environments. A comparative analysis of the wetting behaviors of various liquids at the interface between SiO$_2$/Si and α-MoO$_3$ systems was conducted. The as-prepared samples are ready for mechanical testing after removing residual solvents. The anisotropic mechanical properties of α-MoO$_3$ sheets were systematically investigated using a nanomechanical tensile testing device during scanning electron microscopy (SEM). The derived mechanical properties of α-MoO$_3$ nanosheets revealed orientation dependence, with an anisotropic factor of Young's modulus reaching 1.64. We observed the apparent size dependence of Young's modulus and fracture strength values of α-MoO$_3$. Additionally, the fracture behaviors of α-MoO$_3$ were studied along two orthogonal axes. Our work not only provides important insights into the anisotropic mechanical properties and failure mechanism of α-MoO$_3$, but will also be helpful in the transfer of other multilayer 2D nanosheets directly without the presence of an additional polymer layer.

Results and discussion

Fig. 1a shows the schematic diagram of the α-MoO$_3$ layered crystal structure, where a bilayer distorted MoO$_6$ octahedron forms edge-sharing zigzag rows along the [001] direction (c-axis) and corner-sharing armchair rows along the [100] direction (a-axis). Along the [010] direction (b-axis), the multilayer α-MoO$_3$ nanosheets are held together by weak van der Waals forces. In detail, there are three different types of oxygen atoms within the distorted octahedron, including the terminal oxygen (O$_1$) bonding to the Mo atom in the b-axis direction, the asymmetric oxygen (O$_2$) bonding to two neighboring Mo atoms having different lengths along the a-axis direction, and the symmetric oxygen (O$_3$) forming bonds with two equal Mo atoms in the c-axis and a bond in the b-axis. The reported lattice constants of MoO$_3$ are, respectively, $a = 3.963$ Å, $b = 13.860$ Å, and $c = 3.697$ Å (JCPDS file: 05-0508).[2,27,28]

The α-MoO$_3$ nanosheets were prepared by the mechanical exfoliation method with thicknesses in a range from 20 to 500 nm. As shown in Fig. 1b, the exfoliated α-MoO$_3$ nanosheets with their rectangular shape preferentially tear along the c-axis due to the energy release along the c-axis being much greater than that along the a-axis.[6] To further verify this favored orientation, high-resolution transmission electron microscopy (HRTEM) was employed to characterize the crystal orientation and lattice spacings, as shown in Fig. 1c and d. In detail, the lattice spacing of orthorhombic α-MoO$_3$ is

0.38 nm along the c-axis and 0.39 nm along the a-axis, respectively, which agrees well with the distances of [001] and [100] lattice planes. The selected area electron diffraction (SAED) pattern shown in Fig. 1e reveals the single-crystalline nature of the sample.

As a non-destructive method, angle-resolved polarized micro-Raman spectroscopy (ARPRS) was employed to determine the crystal orientation at the microscopic level.[29,30] Fig. 1f presents the polarized Raman spectrum of an individual MoO$_3$ nanosheet. The peaks centered at 114 cm^{-1} and 283 cm^{-1} are assigned to B$_{2g}$ modes. The peak centered at 158 cm^{-1} is assigned to the A$_g^c$ mode, which originates from the translation vibration of the rigid MoO$_6$ octahedral chains along the c-axis. The peak centered at 818 cm^{-1} (A$_g^a$ mode) reflects the asymmetric stretching vibration of O–Mo–O atoms along the a-axis.[31,32] The polar plots and fittings of normalized Raman intensities of A$_g^c$ and A$_g^a$ modes as a function of sample rotation angle θ are shown in Fig. 1g and h. The intensity of both A$_g^c$ and A$_g^a$ modes exhibits clear dependence on the inclined angle θ, where θ represents the angle between incident polarization and the a-axis. Specifically, the A$_g^c$ mode reaches local maximum along the c-axis while the A$_g^a$ mode reaches local maximum along the a-axis. These two modes can be well fitted to $I(A_g) \propto (A\cos^2\theta + C\sin^2\theta)^2$, which is the detailed calculation process for the anisotropy of Raman signals presented in section S1.† Thus, we would employ A$_g^c$ and A$_g^a$ modes to identify the crystal orientation of the samples.

Owing to the extra-low bending stiffness of few-layer thick 2D nanosheets, a polymer assisted method has been widely employed to transfer the individual 2D nanosheets from the initial substrate to the target substrate. After suitably positioning the test sample, the supported polymer layer has to be removed by either thermal annealing or acetone washing.[14,24] Unfortunately, the presence of residual polymer acting as contamination would greatly deteriorate the mechanical performance of 2D materials.[33–35] Here, we develop a facile method to directly transfer 2D materials to the PTP devices. Fig. 2a presents the schematic drawing of the capillary force-assisted peeling method, where the α-MoO$_3$ nanosheets are directly exported onto the SiO$_2$/Si substrate. To facilitate the manipulation of individual α-MoO$_3$ nanosheets, the whole substrate was immersed in a liquid solution (e.g., water (H$_2$O), ethanol (EtOH) and isopropanol (IPA)). The micro-probe was utilized to slightly detach the edge of the MoO$_3$ nanosheet from the substrate. Meanwhile, the solvent was gradually entrapped inside the interface to weaken the interfacial adhesion between MoO$_3$ and the SiO$_2$/Si substrate, as presented in Fig. 2b and c. To deeply understand the underlying mechanism of the liquid-assisted transfer methodology, we quantitatively evaluated the changes in the work of adhesion based on an energy analysis.[35–37] Generally, the thermodynamic work of adhesion for the separation of MoO$_3$ nanosheets from the underlying substrate in air can be expressed by eqn (1):

$$W_a^{air} = \gamma_{SiO_2} + \gamma_{MoO_3} - \gamma_{SiO_2-MoO_3} \tag{1}$$
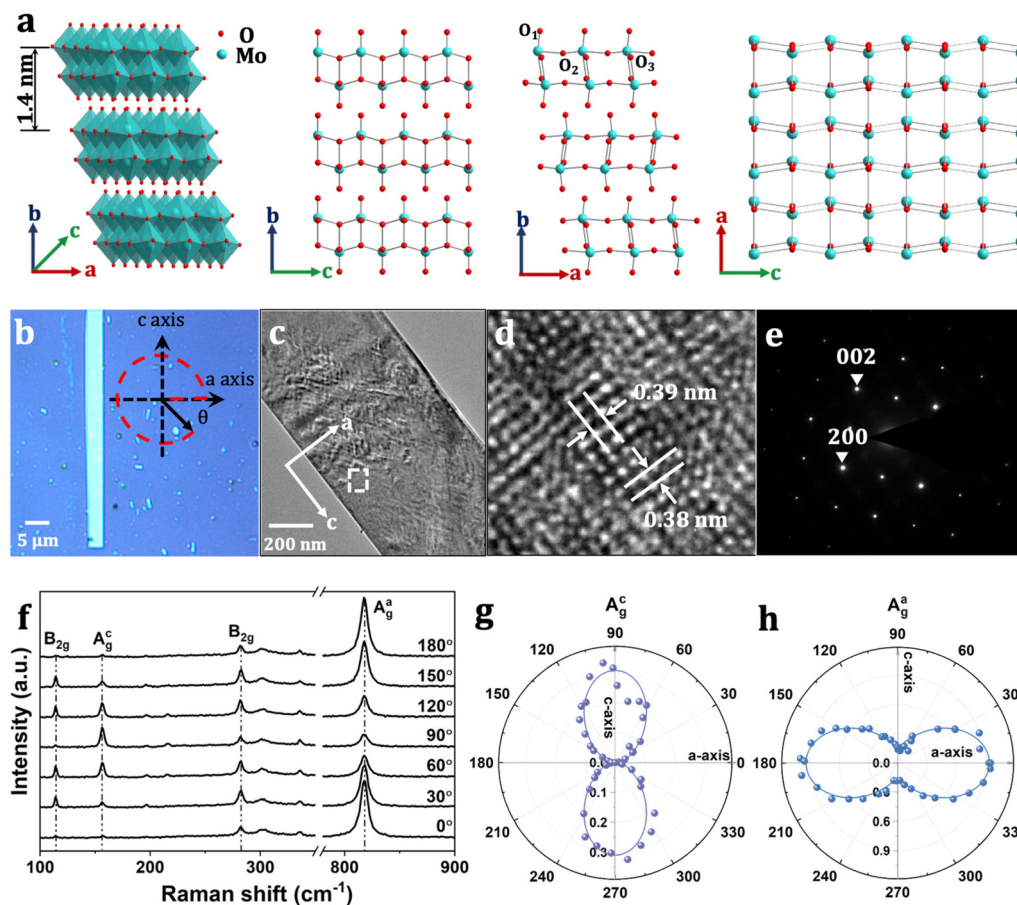
Fig. 1 (a) Schematic diagram of orthorhombic α-MoO_3, where α-MoO_3 nanosheets are packed together by van der Waals interaction along the b-axis, the vertex angle is shared along the a-axis direction and a common edge connection along the c-axis direction. (b) Optical picture of α-MoO_3, with an angle of 0° to the vertical edge. (c) Low magnification TEM image of mechanically exfoliated α-MoO_3 nanosheets. (d) HRTEM image of α-MoO_3. (e) Selected area electron diffraction pattern of α-MoO_3. (f) Raman spectra at different angles with respect to the vertical axis of α-MoO_3. (g and h) Theoretical (solid lines) and experimental (circles) profiles for angle-resolved normalized Raman intensities of A_g^c and A_g^a modes, respectively.
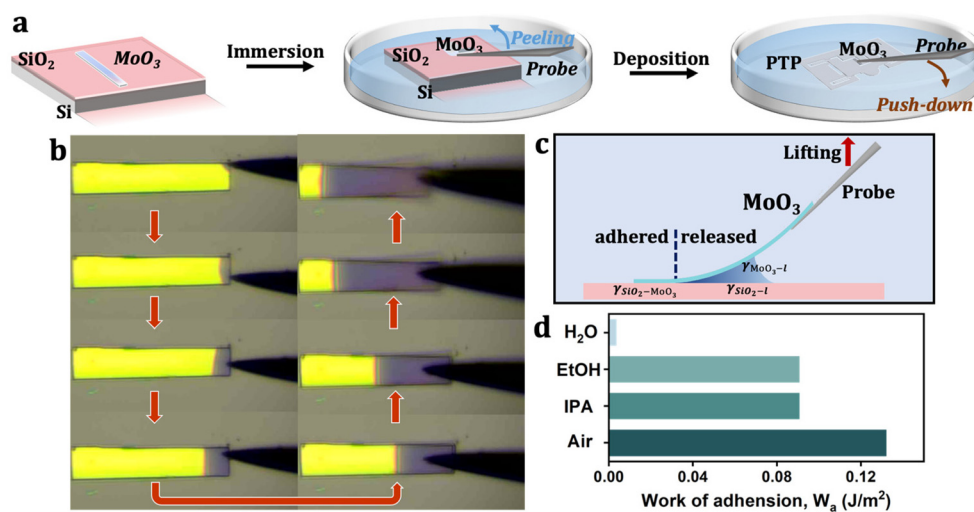

Fig. 2 (a) Schematic diagram of the transfer process. (b) Peeling α-MoO_3 progressively with a probe in a liquid environment. (c) Schematic diagram of the liquid wetting interface in the capillary peeling experiment. (d) Calculated thermodynamic work of adhesion, W_a, in different liquid environments.

where, γ_{SiO_2} and γ_{MoO_3} are the free energies of the SiO$_2$/Si substrate and MoO$_3$, respectively. $\gamma_{SiO_2-MoO_3}$ represents the free energy of the SiO$_2$–MoO$_3$ interface. Once the air medium has been replaced by certain types of solvents, and the whole substrate is correspondingly immersed in a liquid environment, the thermodynamic work, W_a^{liquid}, can be expressed by eqn (2):

$$W_a^{liquid} = \gamma_{SiO_2\text{-}l} + \gamma_{MoO_3\text{-}l} - \gamma_{SiO_2-MoO_3} \qquad (2)$$

where $\gamma_{SiO_2\text{-}l}$ and $\gamma_{MoO_3\text{-}l}$ are the free energies between the SiO$_2$/Si substrate and liquid, and MoO$_3$ and liquid, respectively.

According to the Young–Dupré equation, the adhesion work in the liquid environment depends on the liquid surface energy (γ_l) and contact angles on the SiO$_2$/Si substrate and MoO$_3$ surface:

$$W_a^{liquid} = W_a^{air} - \gamma_1(\cos\theta_{SiO_2} + \cos\theta_{MoO_3}) \qquad (3)$$

where θ_{SiO_2} is the contact angle between the substrate and the liquid, and θ_{MoO_3} is the contact angle between MoO$_3$ and the liquid. The free energies of the SiO$_2$ (γ_{SiO_2}), MoO$_3$ (γ_{MoO_3}) and substrate–MoO$_3$ ($\gamma_{SiO_2-MoO_3}$) interfaces can be derived *via* the Owens Wendt model and Young–Dupré equation.[38,39] Detailed information is presented in the ESI section S2.†

Fig. 2d compares the calculated values of the work of adhesion of the SiO$_2$/Si substrate and MoO$_3$ in air, EtOH, IPA and H$_2$O. Apparently, the work of adhesion shows dependence on the liquids employed. The decreased trend of work of adhesion between the SiO$_2$/Si substrate and the MoO$_3$ from 0.132 to 0.0036 J m^{-2} (an ~37-fold decrease in H$_2$O) was observed. The quantitative analysis described above revealed the underlying mechanism of the capillary force-assisted peeling process. In addition, the wetting behavior of the device also plays an important role in the deposition step. Fig. S3a and b† show the contact angles of the PTP devices with and without O$_2$ plasma treatment. The hydrophilic surface (contact angle below 90°) facilitated the deposition of MoO$_3$ nanosheets onto the substrate, whereas the hydrophobic surface weakened the interaction between the MoO$_3$ nanosheets and the substrate (contact angle above 90°). Eventually, the MoO$_3$ nanosheet was successfully transferred to the plasma-treated device, followed by air drying (Fig. S4a–c†). It is worth noting that the present transfer method developed in our work facilitates the preparation of test samples with high efficiency.

To investigate the mechanical behaviors of multilayer MoO$_3$ nanosheets, uniaxial tensile strength tests were conducted through an *in situ* nanomechanical testing system during SEM (Fig. 3a). The pico-indenter pushes the freestanding part of the device to induce uniaxial stretching with a constant strain rate 1 nm s^{-1}. Meanwhile, the force is recorded by the sensor and the whole deformation process is simultaneously recorded. The thickness of MoO$_3$ nanosheets is measured by AFM (section S5†). It is worth noting that the adhesion between MoO$_3$ and the underlying substrate driven by the vdW interaction is strong enough to firmly clamp the sample without apparent slippage. To support this, we measured the distance between the reference point and the trench edge as shown in Fig. S6a, b and c, d† along two axes, respectively. The consistent length before and after the tensile tests indicated that there was no discernible slippage at the interface.

Fig. 3b presents the typical stress–strain curves of the MoO$_3$ nanosheets along the *c*-axis and *a*-axis, respectively. The linear elasticity of the curves enables us to satisfactorily evaluate Young's modulus along these two axes. As expected, the measured Young's modulus and fracture strength are strongly dependent on the crystalline axes. In detail, the measured Young's modulus and fracture strength along the *c*-axis (91.7 ± 13.7 GPa and 2.1 ± 0.9 GPa, respectively) are much higher than those along the *a*-axis (55.9 ± 8.6 GPa and 0.8 ± 0.3 GPa, respectively) within a thickness range of 30–50 nm. Detailed information is summarized in Table S3.† The observed anisotropy in the mechanical properties is assigned to the anisotropic crystal structure of MoO$_3$ nanosheets, where the asymmetric O$_2$ atom is covalently connected with two Mo atoms along the *a*-axis while the symmetrical O$_3$ atom bonds to three Mo atoms along the *c*-axis. Furthermore, the derived anisotropy ratio ($E_{c\text{-axis}}/E_{a\text{-axis}}$) of Young's modulus for MoO$_3$ nanosheets within a thickness range of 30–50 nm could reach ~1.64. Comparatively, in-plane anisotropy ratios of various anisotropic 2D materials, including black phosphorene (3.81),[40] As$_2$S$_3$ (3.15),[41,42] TiS$_3$ (1.6),[43] SiP (1.3),[44] SiAs (1.33),[44] SiC (1.17),[45] GeP (1.25)[44] and GeAs (1.2)[44] are summarized in Fig. S7.† Impressively, the anisotropy ratio of Young's modulus of MoO$_3$ is one of the largest reported in 2D materials so far.

Fig. 3c, e and d, f represent the typical SEM images of the MoO$_3$ nanosheets before and after the tensile tests along the *c*-axis and *a*-axis, respectively. Similar to other 2D materials (*e.g.*, graphene, MoS$_2$, MoSe$_2$), the MoO$_3$ nanosheets exhibited brittle fracture with a smooth crack front. Due to the in-plane orthogonal structure of MoO$_3$, the crack could catastrophically propagate along the lattice orientation, leading to a similar fracture edge along the two axes.

Earlier works have stated that the mechanical properties of 2D materials, such as graphene, graphene oxide (GO) and MoS$_2$, are highly influenced by their size.[46–48] For example, an apparent decrease in modulus and fracture strength of graphene nanosheets was observed, stemming from inevitable interlayer slippage between adjacent layers during the indentation process.[49] Furthermore, for GO and MoS$_2$ nanosheets, a similar decreasing trend was observed with increasing sample thickness.[47,48] MoO$_3$ nanosheets are expected to exhibit a similar size effect along the two axes. Fig. 3g shows an apparent decrease in Young's modulus (along the *c*-axis) with increasing thickness from 30 nm to 150 nm. Comparatively, as the thickness varied in a relatively large range from 30 nm to 600 nm (a twenty-fold increase), Young's modulus (along the *a*-axis) exhibited a significantly decreasing trend (Fig. 3h). Furthermore, the fracture strength also presented a similar trend. Upon increasing the cross-sectional area (thickness multiplied by width) from 0 to 0.3 μm^2, a slight decrease in the fracture strength (along the *c*-axis) was observed (Fig. S8a†). In contrast, within a larger range (from 0 to 7 μm^2), the fracture
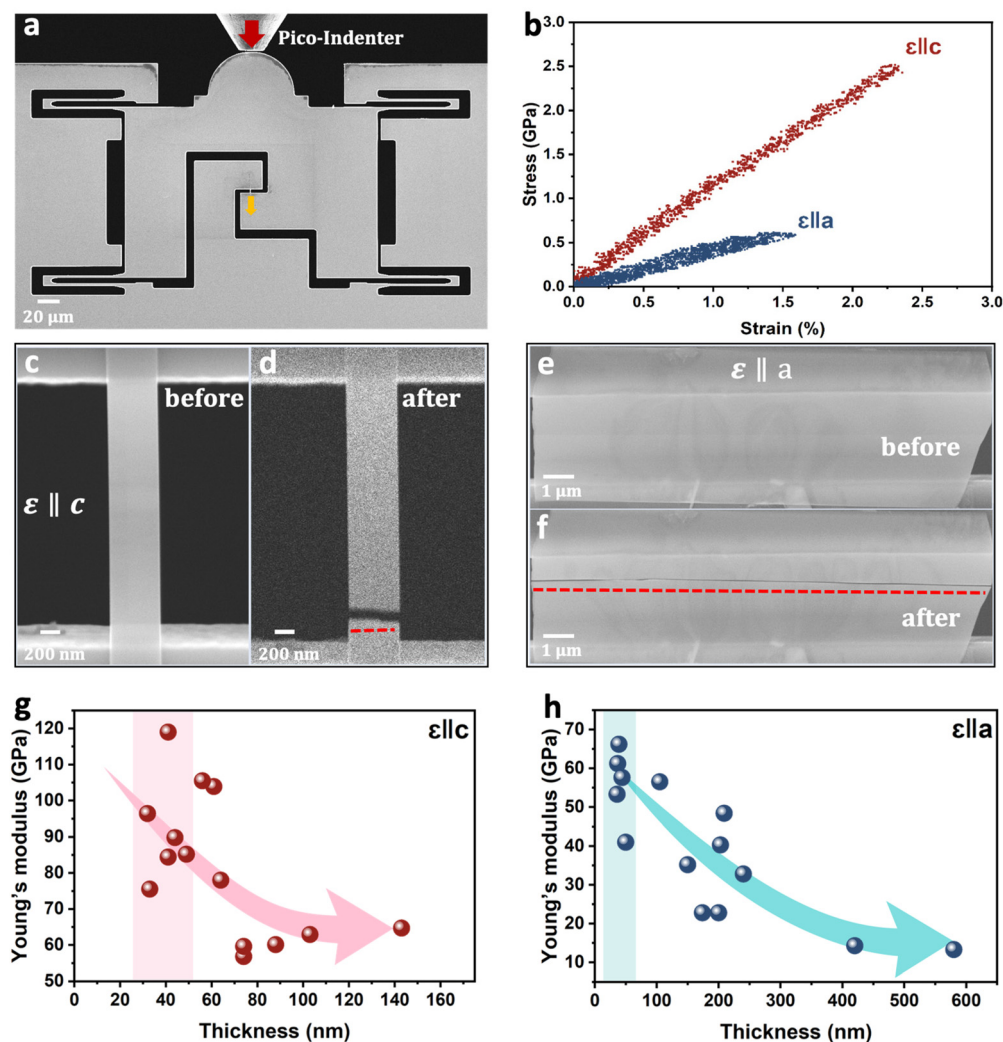
Fig. 3 (a) Nanomechanical device (PTP) and a pico-indenter. (b) Typical tensile stress–strain curves along two orthogonal directions. The derived Young's modulus along the *c*-axis is 103.9 GPa and along the *a*-axis is 41.0 GPa. (c and d) Snapshots of MoO_3 nanosheets before and after loading along the *c*-axis. (e and f) Snapshots of MoO_3 before and after loading along the *a*-axis. The dependence of Young's modulus of MoO_3 nanosheets on sample thickness: along the *c*-axis (g) and *a*-axis (h). The arrows are plotted to guide the eye.

strength (along the *a*-axis) demonstrated a significant decline as the cross-sectional area increased (Fig. S8b†). As mentioned earlier, owing to its high mechanical anisotropy, the most exfoliated MoO_3 nanosheets appeared as ribbon-like structures with length direction along the *c*-axis. Typically, the length of exfoliated samples is around 10–50 µm and the width is around 0.6–5 µm. As a consequence, experimentally, it is hard to directly obtain the ribbon-like samples along the *a*-axis. Instead, the width of tested samples is in a range of several hundreds of nanometers to several tens of micrometers. To exclude the sample size influence on Young's modulus, we also employed FIB to trim the exfoliated sample to strips 1.6 µm in width with stretching direction along the *a*-axis, as shown in Fig. S9a.† For FIB-trimmed samples with a thickness of 96 nm, the measured Young's modulus along the *a*-axis is 44.7 GPa, which is close to that of sample #6 with thickness of

105 nm along the *a*-axis (61.2 GPa). Therefore, the impact of width on Young's modulus is negligible.

Unlike the observable failure process in the stretched mono- or few-layer thick 2D materials (*e.g.*, graphene, MoS_2 and $MoSe_2$),[13,24,48,50] we were unable to capture the crack initiation and propagation during SEM owing to the high speed of crack growth. To reveal the underlying failure mechanism, TEM was employed to characterize the fracture morphology. Fig. 4a and b show the smooth edges of fractured MoO_3 nanosheets roughly along the *c*-axis and *a*-axis, respectively. The observation of the obvious layer step around the fractured edges indicated the poor interlayer interaction, further proving the interplanar fracture-dominated failure mode. Earlier work has proven the transition of fracture modes from intraplanar failure to interplanar failure for MoS_2 once the layer thickness increases from a few nanometers to several
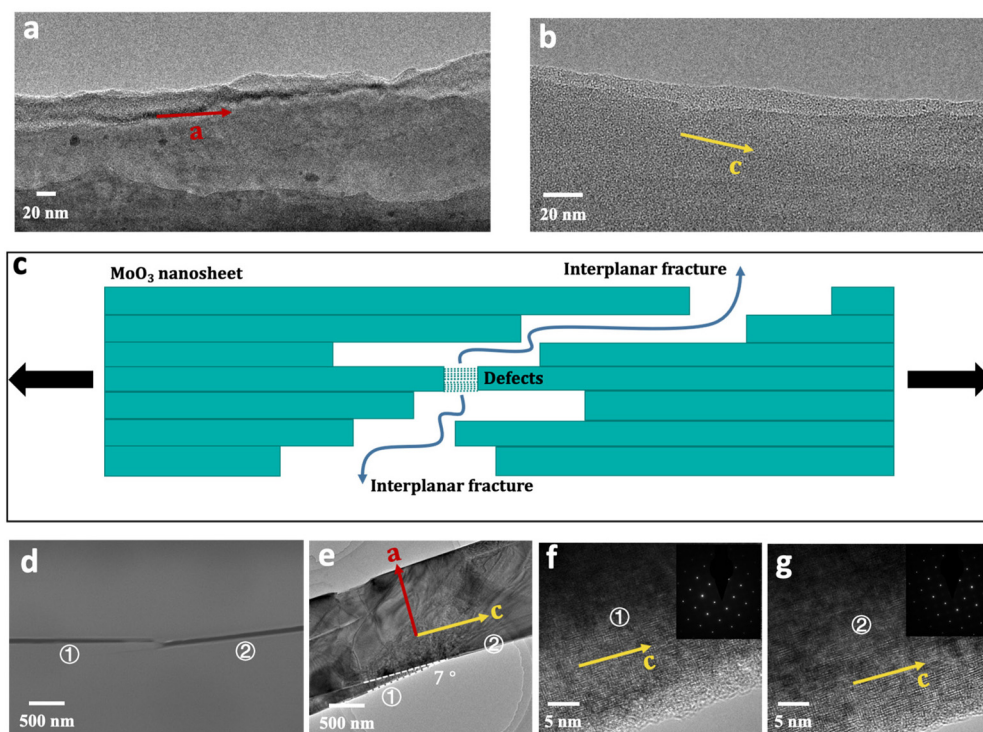
Fig. 4 (a and b) TEM images of the fracture morphology along the c-axis and a-axis, respectively. (c) Schematic illustration of the fracture mode of the MoO_3 nanosheet. (d) SEM image of the observable crack deflection. (e) TEM image of the fracture morphology along the a-axis. (f and g) HRTEM images of MoO_3 in ① and ②. Inset: Selected area electron diffraction pattern.

hundred nanometers.[48] During the tensile process, the presence of defects or incomplete sheets within the MoO_3 nanosheets would easily induce stress concentration, followed by the crack penetrating the whole cross-section of stretched nanosheets, and finally the sudden brittle fracture occurred in the width direction as shown in the schematic of Fig. 4c. Additionally, we also observed the slight crack deflection when nanosheets were stretched along the a-axis, as presented in Fig. 4d. TEM characterization of the deflected point shown in Fig. 4e–g proves that the fracture path is not exactly along the c-axis with a tilted angle of around 7°. Generally, the deflected crack path enables materials to dissipate more energy, leading to their relatively large fracture strength as well as toughness.[7,12] For example, arising from asymmetric edge elastic properties, the stable crack propagation with a deflected and branched path endows a monolayer h-BN nanosheet with high fracture toughness far beyond that given by Griffith's law.[12] Herein, the small tilted angle together with catastrophic failure proves the brittleness of MoO_3 nanosheets.

substrate to facilitate the detachment of nanosheets. The approach developed in the present work not only efficiently avoids the contamination caused by the conventional polymer-assisted transfer method, but also enhances the efficiency of preparing test specimens. Furthermore, we systematically investigated the mechanical properties of multi-layered MoO_3 nanosheets as well as their size dependence along two axes. The Young's modulus of MoO_3 significantly decreases with increasing thickness. In the same thickness range, the derived Young's modulus and fracture strength along the c-axis (91.7 ± 13.7 GPa and 2.1 ± 0.9 GPa, respectively) are much higher than those along the a-axis (55.9 ± 8.6 GPa and 0.8 ± 0.3 GPa, respectively). The derived anisotropy ratio reaches ~1.64, which can be assigned to its crystal structure. Additionally, the multilayer MoO_3 shows a brittle fracture mode with apparent interlayer slippage. Our work provides a basic understanding of the application of MoO_3 in electronic and optoelectronic devices.

Conclusions

In summary, we developed a facile liquid-assisted transfer approach to directly transfer MoO_3 nanosheets onto PTP devices in a liquid environment. The trapped H_2O can greatly reduce the adhesion energy between MoO_3 and the SiO_2/Si

Experimental section

Materials preparation and characterization

MoO_3 nanosheets were mechanically cleaved from their bulk using Scotch tape. The Si wafers with a 300 nm SiO_2 capping layer were processed using oxygen plasma (CPA-A, CIF) before transferring MoO_3. Optical microscopy was used to prelimina-

rily determine the crystal orientation and this was further confirmed by micro-Raman spectroscopy (Renishaw inVia plus). TEM images and SAED patterns were recorded to characterize the lattice structure using a field emission FEI Tecnai G2 F20 microscope (FEI, USA) operated at 200 kV. The AFM (Multimode 8HR, Bruker), in the standard tapping mode, was used to measure the thickness of MoO_3.

Contact angle measurements

We measured the water contact angle on both plasma-treated and untreated devices. MoO_3 crystals and the SiO_2/Si substrate were utilized to measure their contact angles within different liquids (H_2O, EtOH and IPA) using a KRUSS DSA100S instrument.

Preparation of MoO_3 for mechanical tensile tests

The transfer of MoO_3 was conducted with the help of a transfer platform (Metatest, E1-T). Solvents such as H_2O, EtOH and IPA would evaporate spontaneously after the PTP devices containing individual MoO_3 nanosheets were removed from their liquid environment.

Tensile testing

MoO_3 on the PTP device was tested using a Hysitron pico-indenter (PI85) inside a JC-Zeiss Merlin SEM. A diamond indenter can push the PTP device and the load force and displacement were recorded using the transducer. The stretching rate was set at 1 nm s^{-1} to realize quasi-static loading. The real displacement of the sample in the tensile process is read through video using the program code we wrote. The fractured MoO_3 was characterized by TEM using an FEI Tecnai G2 F20 microscope (FEI, USA).

Conflicts of interest

The authors declare no competing financial interest in this work.

Acknowledgements

References

1 V. V. Atuchin, T. A. Gavrilova, T. I. Grigorieva, N. V. Kuratieva, K. A. Okotrub, N. V. Pervukhina and N. V. Surovtsev, *J. Cryst. Growth*, 2011, **318**, 987–990.

2 K. Kalantar-zadeh, J. Tang, M. Wang, K. L. Wang, A. Shailos, K. Galatsis, R. Kojima, V. Strong, A. Lech, W. Wlodarski and R. B. Kaner, *Nanoscale*, 2010, **2**, 429–433.

3 S. Balendhran, S. Walia, H. Nili, J. Z. Ou, S. Zhuiykov, R. B. Kaner, S. Sriram, M. Bhaskaran and K. Kalantar-zadeh, *Adv. Funct. Mater.*, 2013, **23**, 3952–3970.

4 A. V. Avani and E. I. Anila, *Int. J. Hydrogen Energy*, 2022, **47**, 20475–20493.

5 D. K. Choi, D. H. Kim, C. M. Lee, H. Hafeez, S. Sarker, J. S. Yang, H. J. Chae, G. W. Jeong, D. H. Choi, T. W. Kim, S. Yoo, J. Song, B. S. Ma, T. S. Kim, C. H. Kim, H. J. Lee, J. W. Lee, D. Kim, T. S. Bae, S. M. Yu, Y. C. Kang, J. Park, K. H. Kim, M. Sujak, M. Song, C. S. Kim and S. Y. Ryu, *Nat. Commun.*, 2021, **12**, 2864.

6 S. Puebla, R. D'Agosta, G. Sanchez-Santolino, R. Frisenda, C. Munuera and A. Castellanos-Gomez, *npj 2D Mater. Appl.*, 2021, **5**, 37.

7 J. K. Qin, C. Sui, Z. Qin, J. Wu, H. Guo, L. Zhen, C. Y. Xu, Y. Chai, C. Wang, X. He, P. D. Ye and J. Lou, *Nano Lett.*, 2021, **21**, 8043–8050.

8 C. Lee, X. Wei, J. W. Kysar and J. Hone, *Science*, 2008, **321**, 385–388.

9 A. Zandiatashbar, G. H. Lee, S. J. An, S. Lee, N. Mathew, M. Terrones, T. Hayashi, C. R. Picu, J. Hone and N. Koratkar, *Nat. Commun.*, 2014, **5**, 3186.

10 L. Mao, H. Park, R. A. Soler-Crespo, H. D. Espinosa, T. H. Han, S. T. Nguyen and J. Huang, *Nat. Commun.*, 2019, **10**, 3677.

11 H. I. Rasool, C. Ophus, W. S. Klug, A. Zettl and J. K. Gimzewski, *Nat. Commun.*, 2013, **4**, 2811.

12 Y. Yang, Z. Song, G. Lu, Q. Zhang, B. Zhang, B. Ni, C. Wang, X. Li, L. Gu, X. Xie, H. Gao and J. Lou, *Nature*, 2021, **594**, 57–61.

13 P. Zhang, L. Ma, F. Fan, Z. Zeng, C. Peng, P. E. Loya, Z. Liu, Y. Gong, J. Zhang, X. Zhang, P. M. Ajayan, T. Zhu and J. Lou, *Nat. Commun.*, 2014, **5**, 3782.

14 K. Cao, S. Feng, Y. Han, L. Gao, T. Hue Ly, Z. Xu and Y. Lu, *Nat. Commun.*, 2020, **11**, 284.

15 S. P. Koenig, N. G. Boddeti, M. L. Dunn and J. S. Bunch, *Nat. Nanotechnol.*, 2011, **6**, 543–546.

16 G. Wang, Z. Dai, Y. Wang, P. Tan, L. Liu, Z. Xu, Y. Wei, R. Huang and Z. Zhang, *Phys. Rev. Lett.*, 2017, **119**, 036101.

17 G. Wang, Z. Dai, J. Xiao, S. Feng, C. Weng, L. Liu, Z. Xu, R. Huang and Z. Zhang, *Phys. Rev. Lett.*, 2019, **123**, 116101.

18 R. J. T. Nicholl, N. V. Lavrik, I. Vlassiouk, B. R. Srijanto and K. I. Bolotin, *Phys. Rev. Lett.*, 2017, **118**, 266101.

19 N. Iguiniz, R. Frisenda, R. Bratschitsch and A. Castellanos-Gomez, *Adv. Mater.*, 2019, **31**, e1807150.

20 Z. Wang, H. Jia, X. Q. Zheng, R. Yang, G. J. Ye, X. H. Chen and P. X. Feng, *Nano Lett.*, 2016, **16**, 5394–5400.

21 D. Lloyd, X. Liu, N. Boddeti, L. Cantley, R. Long, M. L. Dunn and J. S. Bunch, *Nano Lett.*, 2017, **17**, 5329–5334.

22 J. S. Bunch, S. S. Verbridge, J. S. Alden, A. M. van der Zande, J. M. Parpia, H. G. Craighead and P. L. McEuen, *Nano Lett.*, 2008, **8**, 2458–2462.

23 B. Jang, A. E. Mag-isa, J.-H. Kim, B. Kim, H.-J. Lee, C.-S. Oh, T. Sumigawa and T. Kitamura, *Extreme Mech. Lett.*, 2017, **14**, 10–15.

24 Y. Yang, X. Li, M. Wen, E. Hacopian, W. Chen, Y. Gong, J. Zhang, B. Li, W. Zhou, P. M. Ajayan, Q. Chen, T. Zhu and J. Lou, *Adv. Mater.*, 2017, **29**, 1604201.

25 Y. Han, S. Feng, K. Cao, Y. Wang, L. Gao, Z. Xu and Y. Lu, *Cell Rep. Phys. Sci.*, 2020, **1**, 100172.

26 T. Hallam, N. C. Berner, C. Yim and G. S. Duesberg, *Adv. Mater. Interfaces*, 2014, **1**, 1400115.

27 A. J. Molina-Mendoza, J. L. Lado, J. O. Island, M. A. Niño, L. Aballe, M. Foerster, F. Y. Bruno, A. López-Moreno, L. Vaquero-Garzon, H. S. J. van der Zant, G. Rubio-Bollinger, N. Agraït, E. M. Pérez, J. Fernández-Rossier and A. Castellanos-Gomez, *Chem. Mater.*, 2016, **28**, 4042–4051.

28 Y. Wang, X. Du, J. Wang, M. Su, X. Wan, H. Meng, W. Xie, J. Xu and P. Liu, *ACS Appl. Mater. Interfaces*, 2017, **9**, 5543–5549.

29 S. A. Ali, A. Irfan, A. Mazumder, S. Balendhran, T. Ahmed, S. Walia and A. Ulhaq, *Appl. Phys. Lett.*, 2021, **119**, 193104.

30 B. Zou, X. Wang, Y. Zhou, Y. Zhou, Y. Wu, T. Xing, Y. He, J. Yang, Y. Chen, P. Ren and H. Sun, *Small*, 2023, **19**, 2206932.

31 W. B. Zhang, Q. Qu and K. Lai, *ACS Appl. Mater. Interfaces*, 2017, **9**, 1702–1709.

32 A. Ratnaparkhe, S. Kumar Radha and W. R. L. Lambrecht, *J. Appl. Phys.*, 2021, **130**, 104302.

33 M. R. Rosenberger, H. J. Chuang, K. M. McCreary, A. T. Hanbicki, S. V. Sivaram and B. T. Jonker, *ACS Appl. Mater. Interfaces*, 2018, **10**, 10379–10387.

34 D. G. Purdie, N. M. Pugno, T. Taniguchi, K. Watanabe, A. C. Ferrari and A. Lombardo, *Nat. Commun.*, 2018, **9**, 5387.

35 Y. Hou, X. Ren, J. Fan, G. Wang, Z. Dai, C. Jin, W. Wang, Y. Zhu, S. Zhang, L. Liu and Z. Zhang, *ACS Appl. Mater. Interfaces*, 2020, **12**, 40958–40967.

36 X. Yang, X. Li, Y. Deng, Y. Wang, G. Liu, C. Wei, H. Li, Z. Wu, Q. Zheng, Z. Chen, Q. Jiang, H. Lu and J. Zhu, *Adv. Funct. Mater.*, 2019, **29**, 1902427.

37 S. Kang, T. Yoon, B. S. Ma, M. S. Cho and T.-S. Kim, *Appl. Surf. Sci.*, 2021, **551**, 149229.

38 D. K. Owens and R. C. Wendt, *J. Appl. Polym. Sci.*, 1969, **13**, 1741–1747.

39 A. Kinloch, *J. Mater. Sci.*, 1980, **15**, 2141–2166.

40 X. Cui, W. Dong, S. Feng, G. Wang, C. Wang, S. Wang, Y. Zhou, X. Qiu, L. Liu, Z. Xu and Z. Zhang, *Small*, 2023, **19**, 2301959.

41 M. Siskins, M. Lee, F. Alijani, M. R. van Blankenstein, D. Davidovikj, H. S. J. van der Zant and P. G. Steeneken, *ACS Nano*, 2019, **13**, 10845–10851.

42 M. Dong, Y. Sun, D. J. Dunstan and D. G. Papageorgiou, *Nanoscale*, 2022, **14**, 7872–7880.

43 J. Zhang, X. Liu, Y. Wen, L. Shi, R. Chen, H. Liu and B. Shan, *ACS Appl. Mater. Interfaces*, 2017, **9**, 2509–2515.

44 B. Mortazavi and T. Rabczuk, *Phys. E*, 2018, **103**, 273–278.

45 A. S. M. J. Islam, M. S. Islam, N. Ferdous, J. Park, A. G. Bhuiyan and A. Hashimoto, *Mater. Res. Express*, 2019, **6**, 125073.

46 P. Li, K. Cao, C. Jiang, S. Xu, L. Gao, X. Xiao and Y. Lu, *Nanotechnology*, 2019, **30**, 475708.

47 C. Cao, M. Daly, B. Chen, J. Y. Howe, C. V. Singh, T. Filleter and Y. Sun, *Nano Lett.*, 2015, **15**, 6528–6534.

48 P. Li, C. Jiang, S. Xu, Y. Zhuang, L. Gao, A. Hu, H. Wang and Y. Lu, *Nanoscale*, 2017, **9**, 9119–9128.

49 A. Falin, Q. Cai, E. J. G. Santos, D. Scullion, D. Qian, R. Zhang, Z. Yang, S. Huang, K. Watanabe, T. Taniguchi, M. R. Barnett, Y. Chen, R. S. Ruoff and L. H. Li, *Nat. Commun.*, 2017, **8**, 15815.

50 B. Jang, B. Kim, J. H. Kim, H. J. Lee, T. Sumigawa and T. Kitamura, *Nanoscale*, 2017, **9**, 17325–17333.